Deformation and Failure Characteristics of Sandstone Subjected to True-Triaxial Unloading: An Experimental and Numerical Study

Xiao Fan[1] ▪ Jiang De-Yi[1*] ▪ Wu Fei[1*] ▪ Chen Jie[1] ▪ Zhang Jian-Zhi[1,2] ▪ Liu Wei[1]

[1] *State Key Laboratory of Coal Mine Disaster Dynamics and Control, School of Resources and Safety Engineering, Chongqing University, Chongqing, 400044, China*

[2] *School of Civil Engineering, Chongqing University, Chongqing, 400045, China*

Abstract: The influence of maximum principal stress level on true-triaxial unloading behaviors and the failure mechanism of sandstone samples were comprehensively investigated by laboratory tests and discrete element simulations. The results show that the level of σ_1 at unloading point significantly affects the deformation and failure characteristics of sandstone samples under true-triaxial unloading conditions. As the level of σ_1 at unloading point increases, the ultimate bearing capacity of sandstone sample is increasingly strengthened, while the sample collapses more easily during the unloading process, and the failure mode of sandstone sample changes from mixed tensile-shear failure to shear failure. With the increase in the level of σ_1 at unloading point, the accumulative micro-cracks at the unloading point and micro-crack generation rate during the unloading phase exhibit an increasing trend, while the sum of micro-cracks at the unloading phase and the ratio between the amount of tensile micro-cracks and shear micro-cracks roughly show a downward trend. The formation of macro fracture in sandstone sample is closely related to the stress conditions and material inhomogeneity. The tensile fracture in the upper right part of sample when the level of σ_1 is relatively low should be attributed to the superiority in tensile contacts between particles in terms of contact number and corresponding tensile force.

Keywords True-triaxial unloading·Discrete element simulations·Maximum principal stress·Failure mechanism

** Correspondence to: D.Y. Jiang; F Wu; School of Resources and Safety Engineering, Chongqing University, Shazheng Road, Shapingba District, Chongqing, PR China; Email: damoy68@163.com; Tel. +86-23-6512-0720; Fax. +86-23-6512-3511

1 Introduction

A growing demand for mineral resources and underground space with the rapid development in society and economy makes underground excavation become more popular. Excavation of rock mass during underground engineering projects irrevocably changes the in-situ stress field of surrounding rocks and may cause different forms of rock failure.[1] For brittle hard rock subjected to high unloading-induced stress, the rock failure near an excavation site can be distinguished into stable failure, such as slabbing, which is characterized by a progressive generation of surface fractures, and unstable failure, such as rockburst, which occurs suddenly with a large quantity of energy release.[2-4] To gain a deep insight into the unloading behavior of a rock mass during underground excavation, many experimental investigations have been carried out on rocks in the laboratory.[5-8] Ding et al[9] carried out conventional triaxial compression and unloading confining pressure tests to investigate the failure behaviors of sandstone after different high temperature treatments. The results showed that brittle failure was more obvious in the unloading confining pressure tests with the increase in initial confining pressure.[9] Huang et al[10] carried out laboratory unloading tests on man-made rock specimens with one or two cracks to explore the rock crack evolution during underground excavation. Zhou et al[11] investigated the unloading failure characteristics of rocks via unloading confining pressure at different levels of unloading points. With the aid of nuclear magnetic resonance (NMR), the meso-damage evolution characteristics of the unloading rock was analyzed. Huang et al[12] conducted triaxial unloading tests on marble specimens and found that the unloading rate and initial confining pressure had significant influence on the strain energy conversion of specimen during the unloading process. Considering that the rock mass in underground engineering was usually located within a three-dimensional stress state before being excavated, researchers turned their attention to carrying out true-triaxial unloading tests on rocks by developing sophisticated true-triaxial apparatuses to better simulate the conversion of three-dimensional stress in practical excavation engineering.[13-14] Li et al[15] investigated the strength and failure modes of cubic rock

specimens under true-triaxial unloading condition using a novel true-triaxial test system and found that the rock strength increased with the intermediate principal stress σ_2. Du et al[16] conducted true-triaxial unloading tests and dynamically disturbed loading tests on three types of rock specimens to reveal the rock failure mechanism and pointed out that the mechanisms that induced slabbing were closely associated with those that triggered rockbursts. He et al[17] examined the rock burst process and acoustic emission characteristics of limestone in the laboratory with a true-triaxial test facility which achieved abrupt unloading of the minimum principal stress σ_3 in one loading face. Zhao et al[18] investigated the influence of unloading rate on the strainburst behavior of Beishan granite and revealed that the failure mode of rock samples changed from strainburst to spalling as the unloading rate decreased.

Since researches on the mechanical behaviors of rocks under unloading conditions have been extensively reported, most of them focus on the factors like unloading rate, initial confining pressure that significantly influenced the failure mode and mechanical properties, the maximum principal stress level at the initial unloading point is rarely considered as a researching point in true-triaxial unloading tests.[19] Actually, in underground engineering projects, due to human activities, it is likely that stress concentration occurred earlier in a rock mass before the rock mass was involved in the excavation scheme. An example for this is adjacent tunnels in the excavating sequence of time. The tunnel under construction may cause stress concentration in the nearby rock masses linked with other tunnels.[20] Therefore, it is worth examining the influence of maximum principal stress level on subsequent rock unloading behaviors for evaluating the unloading failure characteristics of rock mass where stress concentration occurs before excavation.

The laboratory experimental studies have promoted the understanding of macro mechanical behaviors and failure characteristics of rocks. However, it is difficult to directly visualize the micro-crack generation and underling stress field of rocks by experiment investigation.[21] To identify the variation of microstructures and stress distribution in rocks under different loading conditions, some numerical methods,

such as finite element method (FEM)[22], boundary element method (BEM)[23], discrete element method (DEM)[24], have been adopted by researchers. Compared with the numerical methods based on the theory of continuum mechanics, DEM is a promising approach for dealing with discontinuity problems and tracking the microstructures in the failure process.[25] By means of DEM, Yang et al. revealed the crack evolution mechanism in brittle sandstone containing non-coplanar fissures under uniaxial compression.[26] Hazzard and Young[27] firstly simulated the acoustic emissions of a granite sample by using the distinct-element code. Liu et al[28] analyzed the relationships between the characteristic stress thresholds of intact rock and the micro-geometric heterogeneity index with the grain-based models. Park and Min[29] investigated the mechanical behaviors of transversely isotropic rock based on the bonded-particle DEM model. Additionally, extensive DEM simulations were undertaken to estimate the shear behaviors of rock joints in the direct shear tests.[30-33] Moreover, modelling the failure characteristics and mechanical properties of brittle rock under true-triaxial stress state by 3D DEM has also been reported recently.[34-35] In view of the promising performance of DEM in reproducing the mechanical behaviors and visualizing microscopic cracking process, it is adopted in present study to examine the failure and deformation of rocks under true-triaxial unloading conditions.

In this paper, both laboratory tests and numerical tests were carried out to identify the influence of maximum principal stress level on subsequent unloading behaviors of sandstone samples and elucidate the failure mechanism by analyzing the particle-scale responses. The structure of this paper is as follows. Section 2 introduces the experimental procedures and loading schemes. Section 3 mainly introduces the numerical model generation and related micro-parameter calibration. Section 4 displays the results of laboratory tests and numerical tests and chiefly discusses the microscopic mechanism of rock failure and deformation according to the micro-crack characteristics and particle displacement. Section 5 summarizes this work.

2 Experimental study

2.1 Experimental procedures

The rock material was sandstone obtained from a quarry in Weiyuan county of Sichuan Province, western of China. To reduce the material discreteness, the sandstone samples were extracted from a single rock block without visible cracks, and polished into rectangular prisms with a nominal dimension of 50mm × 50mm × 100mm, as shown in Figure 1. The precision control of samples was exercised according to the standard requirements of ISRM 36, with a surface flatness controlled within ± 0.02mm. Prior to the unloading tests, all the machined samples were dried at 105 °C for 12 hours, and wave velocity measurements were conducted on them with an ultrasonic measuring system to pick out the samples with nearly the same P wave velocity. Subsequently, the true-triaxial experiments on these chosen samples were conducted using the GCTS Triaxial Rock Testing System (RTX-3000), which was capable of applying forces independently in three orthogonal directions. The rock sample was placed into the true-triaxial cell, which contains two pairs of loading plates providing the lateral principal stresses. The axial stress are applied by the rigid loading frame. Additionally, the rock sample deformation in each direction were measured by two parallel linear variable differential transformers (LVDTs) fixed on the true-triaxial cell.

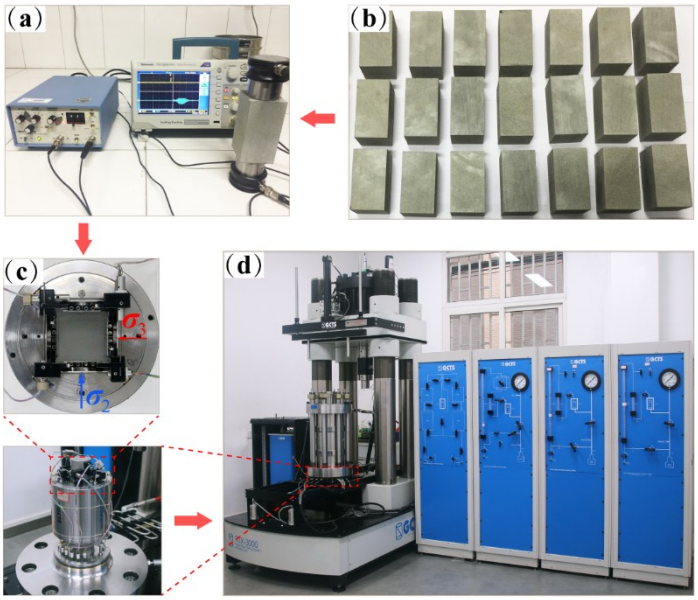

FIGURE 1 Experimental procedures **(a)** ultrasonic measurement **(b)** sample preparation **(c)** putting the sample into a true-triaxial cell **(d)** performing the true-triaxial tests with the GCTS Triaxial Rock Testing System (RTX-3000)

2.2 Loading schemes

To estimate the effect of stress concentration in rock masses on subsequent unloading behaviors, we carried out a series of true-triaxial unloading tests with a stress path considering different maximum principal stress levels, before which the true-triaxial compressive test was performed for the rational selection of maximum principal stress levels relevant to unloading tests. These two kinds of true-triaxial tests were described as follows:

True-triaxial compressive test was conducted primarily to obtain the true-triaxial compressive strength (σ_{1max}). The first step was to raise the stresses (σ_1, σ_2, σ_3) on the surfaces of sample with a rate of 0.1 MPa/s to predefined values (σ_{1i}, σ_{2i}, σ_{3i}) to simulate the initial stress state of rock mass, as shown in Figure 2. Then, keeping σ_2 and σ_3 constant, σ_1 was continuously increased with the rate of 0.1 MPa/s until rock failure eventually occurred.

True-triaxial unloading tests were designed according to the results of true-triaxial compressive test. Firstly, the predefined in situ stresses (σ_{1i}, σ_{2i}, σ_{3i}) were

applied on the surfaces of sample with a rate of 0.1 MPa/s. Subsequently, holding σ_2 and σ_3 constant, σ_1 was raised to σ_{1u} ($\sigma_{1u} = \gamma\sigma_{1max}$, γ denotes the maximum principal stress level parameter) with the rate of 0.1 MPa/s to simulate different degrees of stress concentration or initial damage. After that, σ_2 was held constant. Meanwhile, σ_1 was continuously increased while σ_3 was unloaded at the same rate of 0.1 MPa/s until rock finally failed. The predefined in situ stresses and maximum principal stress levels before unloading phase are shown in Table 1.

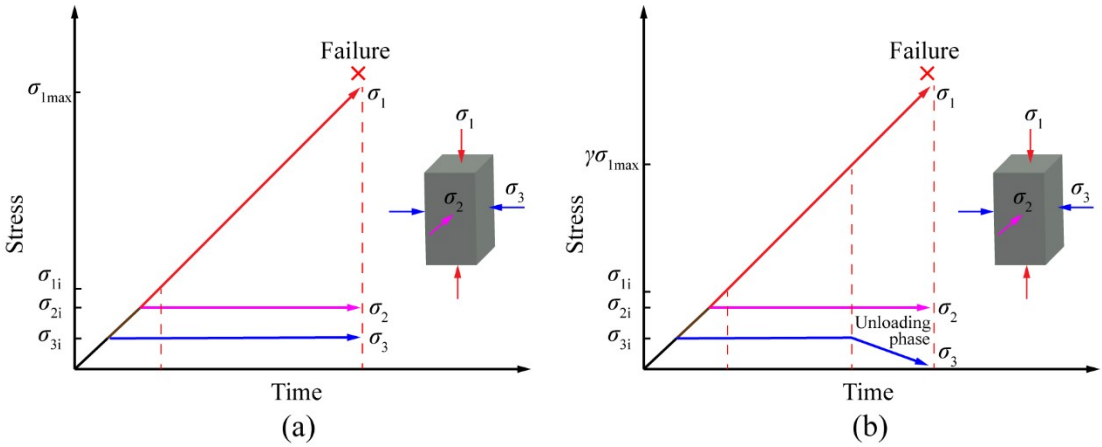

FIGURE 2 Loading schemes (**a)** true-triaxial compressive test **(b)** true-triaxial unloading test

TABLE 1 Specimen number and predefined principal stresses for true-triaxial tests

Test type	Sample no.	σ_{3i}, MPa	σ_{2i}, MPa	σ_{1i}, MPa	σ_{1u}, MPa	σ_{1max}, MPa	$\gamma=\sigma_{1u}/\sigma_{1max}$
True-triaxial compressive test	TC-S-1	20	40	50	-	198	-
True-triaxial unloading test	TU-S-1	20	40	50	139	-	0.70
	TU-S-2	20	40	50	149		0.75
	TU-S-3	20	40	50	159		0.80
	TU-S-4	20	40	50	169		0.85
	TU-S-5	20	40	50	179		0.90
	TU-S-6	20	40	50	189		0.95

3 Numerical model

3.1 Bonded-particle model

In this study, numerical simulations were performed using commercially available Particle Flow Code in three-dimensions (PFC3D) 37, which was one of the platforms based on DEM. In PFC3D, the rock sample was represented by the bonded-particle model (BPM) that was an assemblage of rigid particles bonded at contacts. The linear parallel bond model (LPBM) was applied in the particle contacts. It provided the behavior of two interfaces. The first interface was equivalent to the linear model that included a pair of linear springs with constant normal and shear stiffness, imposing elastic interaction between the pieces. The second interface was named parallel bond, which could be envisioned as a set of elastic springs uniformly distributed over the bond's cross-section. When the parallel bond was created, any relative motion between the contacting pieces would cause the variation of force and moment within the bond material, which were relevant to the maximum normal and shear stress acting on the periphery of the bond. Once the maximum normal stress or shear stress exceeded the bond strength limit, parallel bond broke, and the contact model turned into an unbonded state equivalent to the linear model, as shown in Figure 3. The mechanism of force and moment in parallel bond could be described by Eqs. (1)-(6).

$$\Delta \overline{F}_{n} = \overline{k}_{n} \overline{A} \Delta \delta_{n} \tag{1}$$

$$\Delta \overline{F}_{ss} = \overline{k}_{s} \overline{A} \Delta \delta_{ss} \tag{2}$$

$$\Delta \overline{F}_{st} = \overline{k}_{s} \overline{A} \Delta \delta_{st} \tag{3}$$

$$\Delta \overline{M}_{t} = \overline{k}_{s} \overline{J} \Delta \theta_{t} \tag{4}$$

$$\Delta \overline{M}_{bs} = \overline{k}_{n} \overline{I} \Delta \theta_{bs} \tag{5}$$

$$\Delta \overline{M}_{bt} = \overline{k}_{n} \overline{I} \Delta \theta_{bt} \tag{6}$$

where $\Delta\bar{F}_n$ was the increment of normal parallel-bond force; $\Delta\bar{F}_{ss}$ and $\Delta\bar{F}_{st}$ were components of shear parallel-bond force increment; $\Delta\bar{M}_t$ was the increment of parallel-bond twisting moment; $\Delta\bar{M}_{bs}$ and $\Delta\bar{M}_{bt}$ were components of parallel-bond bending moment increment; $\bar{k}_n$ and $\bar{k}_s$ were normal and shear stiffness of the parallel-bond, respectively; $\Delta\delta_n$ was relative normal-displacement increment; $\Delta\delta_{ss}$ and $\Delta\delta_{st}$ were components of relative shear-displacement increment; $\bar{J}$ and $\bar{I}$ were polar moment and moment of inertia of the parallel-bond cross section, respectively; $\Delta\theta_t$ were relative twist-rotation increment; $\Delta\theta_{bs}$ and $\Delta\theta_{bt}$ components of relative bend-rotation increment; $\bar{A}$ was the cross-sectional area. The maximum normal stress $\bar{\sigma}$ and shear stress $\bar{\tau}$ acting on the parallel-bond periphery could be calculated using Eqs. (7) and (8).

$$\bar{\sigma} = \frac{\bar{F}_n}{\bar{A}} + \bar{\beta}\frac{\left\|\bar{\mathbf{M}}_b\right\|\bar{R}}{\bar{I}} \tag{7}$$

$$\bar{\tau} = \frac{\left\|\bar{\mathbf{F}}_s\right\|}{\bar{A}} + \bar{\beta}\frac{\left|\bar{M}_t\right|\bar{R}}{\bar{J}} \tag{8}$$

where $\bar{\beta}$ was the moment-contribution factor; $\bar{R}$ was the radius of the bonded zone; $\bar{\mathbf{F}}_s$ was the shear parallel-bond force in vector form; $\bar{\mathbf{M}}_b$ was the parallel-bond bending moment in vector form.

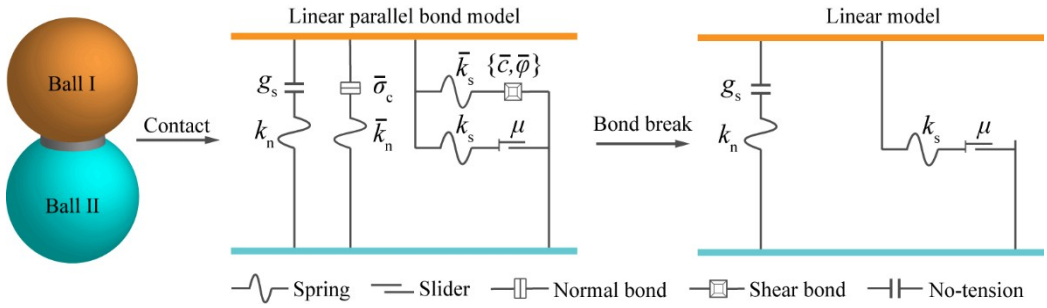

FIGURE 3 Linear parallel bond model

3.2 Model generation and micro-parameter calibration

The macroscopic behaviors of BPM are determined by the micro-parameters characterizing the parallel bonds and particles 38, which cannot be obtained directly from the laboratory experiments. Therefore, these micro-parameters have to be calibrated by comparing the macroscopic behaviors of BPM with that of physical rock sample. By far researchers have developed some parameter calibration methods 39-42, among which trial-and-error method is the most common one. In this study, the true-triaxial compressive test corresponding to the physical experiment was involved in matching the macroscopic behaviors and the micro-parameters were also confirmed by using the trial-and-error method. Firstly, a numerical sandstone sample with a dimension of 50 mm × 50 mm × 100 mm was created. It was composed of 5606 particles, of which the size followed a uniform distribution and ranged from 1.8mm to 2.1mm. The particles were bonded by parallel-bond contacts, as shown in Figure 4. Subsequently, a true-triaxial compressive test with a loading path mimicking above-mentioned laboratory loading scheme (see Figure 2a) was conducted. The desired stresses applied on the numerical sandstone sample were provided by controlling the translational velocities of six walls by using a servo-mechanism. Based on this test, the micro-parameter calibration was implemented. The macroscopic responses including stress-strain curves and failure mode were used to calibrate the micro-parameters after each trial. This process was repeated until the macroscopic responses achieved a good agreement with previous experimental observations. Table 2 presents

the calibrated micro-parameters for Weiyuan sandstone sample. Figure 4 shows the comparison between the final results of numerical and experimental tests. It can be observed that the numerically predicted stress-strain curves and failure mode coincide with the experimental observations, which proves that the calibrated micro-parameters are capable of reproducing the mechanical and failure behaviors of sandstone under true-triaxial conditions.

To further explore the grain-scale responses of sandstone sample under true-triaxial unloading conditions, we performed true-triaxial unloading tests on the numerical sandstone sample with these calibrated micro-parameters. The unloading path in numerical simulation was consistent with that used in above-mentioned experimental tests (see Figure 2b), in which the maximum principal stress level was taken as a primary factor influencing the unloading behaviors of rock samples. In the next section, the micro-crack characteristics, distribution of ball displacement and failure process were investigated to enhance our understanding in mesoscopic mechanical behaviors of sandstone.

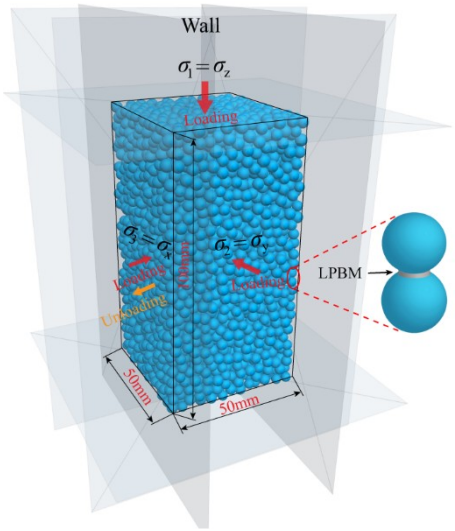

FIGURE 4 Numerical sandstone specimen

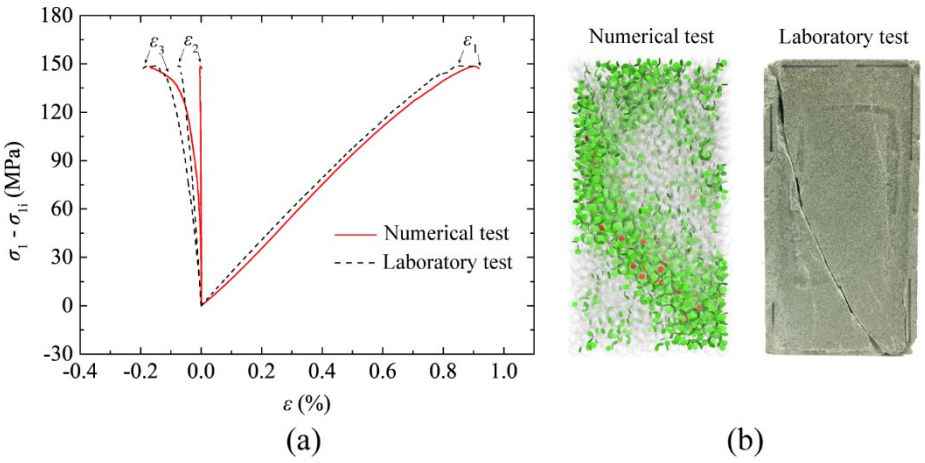

FIGURE 5 Comparison of DEM simulation results with experimental observations (a) stress-strian curves (b) failure modes

TABLE 2 Microscopic parameters of sandstone in the true-triaxial compressive test

Microscopic parameters	Symbol	Value
Particle radius (m)	r	1.8e-3 ~ 2.1e-3
Particle density (kg/m^3)	ρ	2370
Friction coefficient	μ(Linear interface)	0.6
Parallel bond tensile strength (Pa)	$\bar{\sigma}$	3.1e7
Parallel bond cohesion (Pa)	$\bar{c}$	13.2e7
Parallel bond friction angle (degree)	$\bar{\phi}$	0
Normal-to-shear stiffness ratio	κ*(Linear interface), $\bar{\kappa}$*(Parallel bond interface)	1.38
Young's modulus (Pa)	E*(Linear interface), $\bar{E}$*(Parallel bond interface)	1.36e10

4 Results and discussion

4.1 Macroscopic mechanical behaviors

The rock mechanical properties obtained from the laboratory experiments and numerical simulations are presented in Figure 6. Peak strength in present study refers to the maximum value that the stress difference σ_1-σ_{1i} can reach under true-triaxial unloading conditions, and peak strain is the strain ε_1 corresponding to the peak strength. As seen in Figure 6, the peak strengths simulated by PFC3D with various maximum principal stress level parameters γ are very close to those obtained from laboratory experiments. Similarly, the simulated peak strains generally present a good agreement with the experimental observations. The main difference in peak strain between experiment and simulation is that when γ equals 0.75, the peak strain

measured by experiment is much lower than that predicted by simulation. With the increase in γ, the peak strength and peak strain all exhibit an increasing trend. The trend in peak strength implies that under this true-triaxial unloading condition, the rock bearing capacity is increasingly strengthened with increasing maximum principal stress level at the initial unloading point. The weaker bearing capacity corresponding to a low γ is mainly due to that unloading σ_3 rapidly weakens the rock bearing capacity before the axial stress σ_1 becomes large enough.

Furthermore, to quantitatively analyze the difficulty in the collapse of rock sample under true-triaxial unloading conditions, the minimum principal stress decreasing parameter η involving the decrement in σ_3 within the unloading phase is proposed as follows:

$$\eta = \frac{\sigma_3^{(0)} - \sigma_3^{(p)}}{\sigma_3^{(0)}} \tag{9}$$

where $\sigma_3^{(0)}$ and $\sigma_3^{(p)}$ represent the value of σ_3 at the initial unloading point and peak stress point, respectively. Figure 6c shows the variation of minimum principal stress decreasing parameter η from the experiments and numerical simulation. It can be observed that the numerical values of η are basically similar to those obtained experimentally despite the fact that when γ equals 0.7, the value of η measured by experiment is obviously lower than that predicted by numerical simulation. It should be noted that the parameter η varies inversely with γ both in laboratory and numerical tests, which indicates that a higher level of σ_1 at the initial unloading point will reduce the decrement in σ_3 within the unloading phase. In other words, the rock sample collapses more easily with a higher level of σ_1 at the initial unloading point under this true-triaxial unloading condition. Zhou et al. conducted conventional triaxial unloading tests on marble samples and defined the level of σ_1 at the initial unloading point as unloading intensity. With the aid of NMR system, they found that the unloading intensity had an effect on the number and size of micro-pores in samples during the unloading process 11. One can speculate that in present study the extent of

damage caused by micro-pores may differ in the rock samples at the initial unloading point with different γ, which results in the difference in difficulty of rock failure under true-triaxial unloading conditions with various γ. In addition, at the initial unloading stage, the bearing capacities of rock samples with different γ are almost the same due to close confining pressures. However，at the same time, the sample with a higher γ means that it will achieve the bearing capacity much sooner. That is one of the reasons why the parameter η varies inversely with γ.

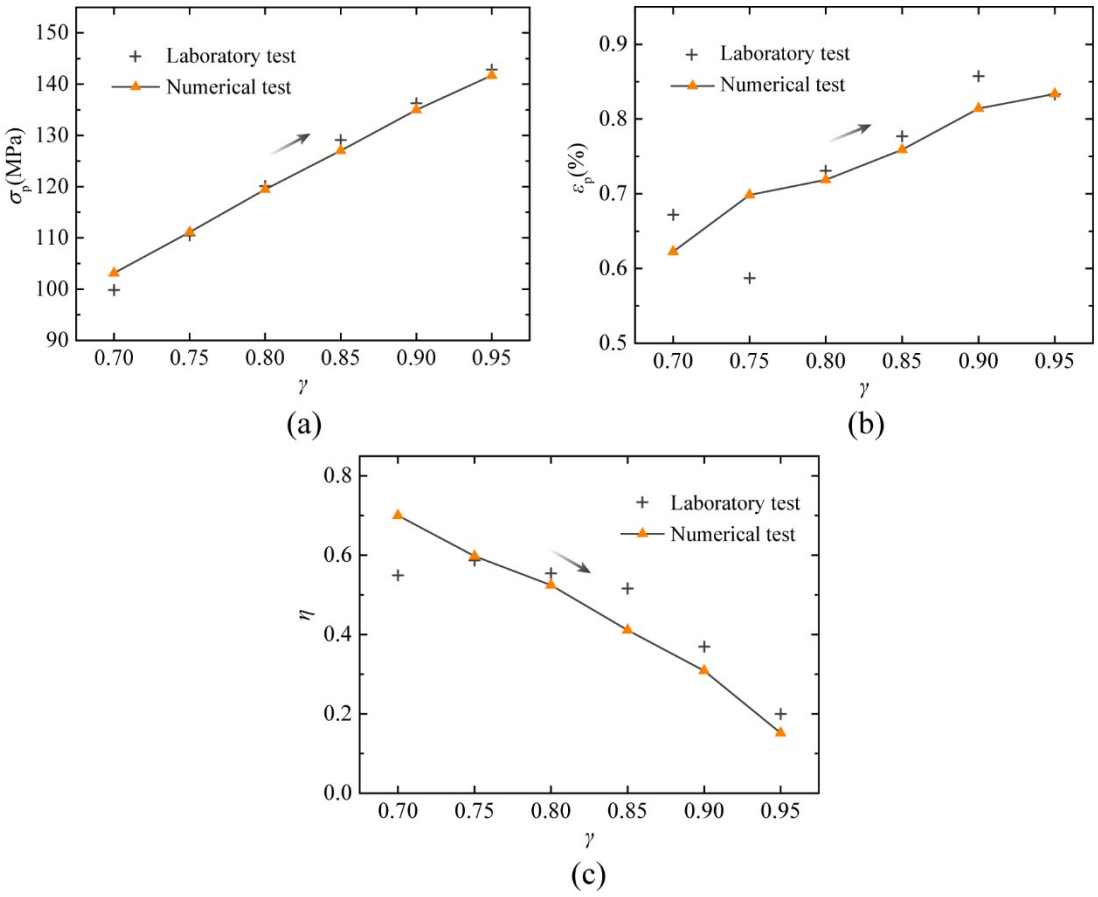

FIGURE 6 Mechanical properties obtained from the laboratory experiments and numerical simulation **(a)** peak strength **(b)** peak strain **(c)** minimum principal stress decreasing parameter

Figure 7 presents the ultimate failure modes of sandstones in the laboratory experiments and numerical simulation. Note that the breakage of parallel bond in PFC3D is marked as green disk (tensile micro-crack) or red disk (shear micro-crack). As seen in Figure 7, all the macro fracture planes of rock samples are approximately parallel to the stress σ_2, which should be attributed to the fact that the samples are less

restricted by force in the direction of σ_3. It can be observed that as $\gamma > 0.75$, the samples in physical experiments fail by shear with one or two oblique fracture plane(s). However, when γ is no more than 0.75, both the oblique shear fracture and approximately vertical tensile fracture can be seen in the physical samples, indicating that the failure mode of samples are mixed tensile and shear failure. Additionally, the shear fracture angles are measured by a protractor, and the results show that they range from 60° to 75°. The distributions of macro fractures in numerical samples are not entirely consistent with those observed in physical samples. It is mainly due to that any component such as mineral particle in a physical sandstone sample is randomly distributed, and the samples are not exactly the same even though they are extracted from a single rock block. In contrast, the randomness of component in the numerical samples for different tests is fixed. We can see that the difference of macro fracture distribution between different numerical samples is not obvious. Similar dominant shear fracture containing most of the micro-cracks can be found in each sample and the relevant fracture angle is about 60°. However, the other macro fracture in the upper-right part of each sample is different from each other. As γ is no more than 0.8, the upper-right fractures are approximately vertical and should be regarded as tensile fractures, but when γ>0.8, they are shear fractures. Briefly, the failure mode of rock sample both in laboratory and numerical tests changes from mixed tensile-shear failure to shear failure with the increase in γ. It is worth noting that when γ is relatively low, tensile fracture appears both in physical and numerical samples, which may be due to that unloading σ_3 is equated with applying a tensile force on the sample in σ_3 direction, as γ is relatively low, the higher decrement in σ_3 within the unloading phase means a larger tensile force applied on the sample.

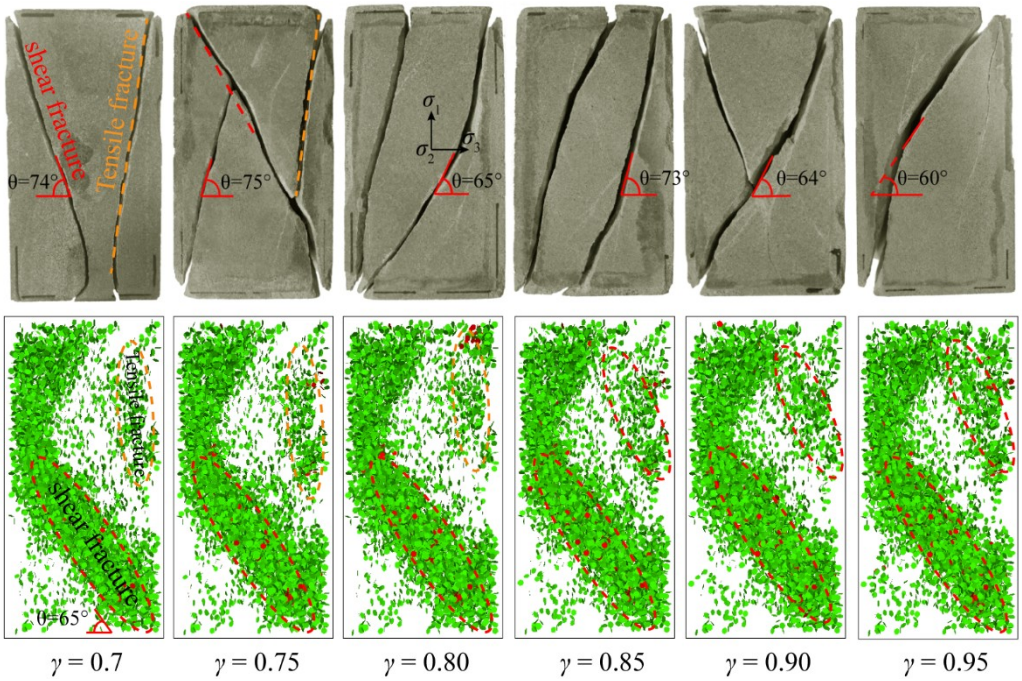

FIGURE 7 Ultimate failure modes of sandstones in the laboratory experiments and numerical simulation

4.2 Number evolution of micro-cracks

Figure 8 presents the stress-strain curves and the evolution of micro-crack number obtained from the numerical simulations. As seen in Figure 8, the curves of total micro-cracks with different γ exhibit similar trends. Take γ = 0.7 as an example, during the simulation, the number of micro-cracks gradually increases with the axial strain. Four characteristic stages can be identified on the curve of total micro-cracks according to the increasing rate of micro-cracks. Stage I corresponds to the compaction phase of rock sample, and no micro-crack occurs at this stage. Stage II is generally associated with the phase of linear elastic deformation. At this stage, a few micro-cracks can be observed and the temporal distribution of micro-crack is relatively uniform. Stage III is coincident with the unloading phase. It can be seen that the micro-crack count rate rises suddenly and the curve of total micro-cracks starts to bend upward, which indicates that the internal damage of rock sample increases rapidly during this stage. Stage IV corresponds to the post-peak stage. We can see that

the rock sample experiences a sharp growth in micro-crack number again and the count rate in this phase is much larger than that at former stages, denoting the sudden appearance of macroscopic fractures after the peak stress point.

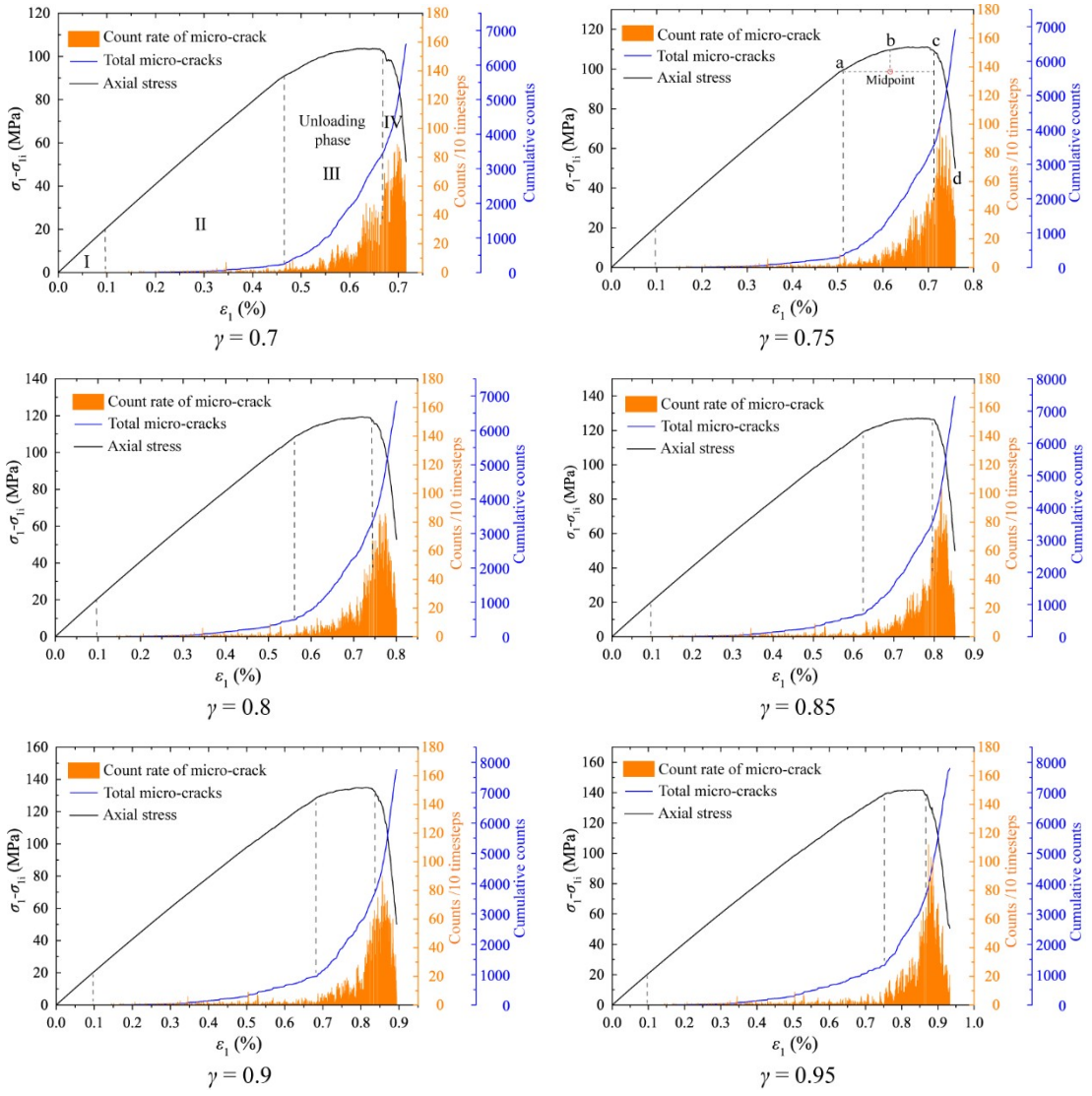

FIGURE 8 Number evolution of micro-cracks in the numerical simulation of true-triaxial unloading tests

Figure 9 displays some other information about micro-crack number influenced by the maximum principal stress level parameter γ. As seen in Figure 9a, the number of accumulative micro-cracks at the starting point of unloading phase increases with γ, which indicates under true-triaxial compressive conditions, damage accumulates in the rock sample as the stress σ_1 grows. In other words, a higher σ_1 at the starting point of unloading phase causes more damage in the rock sample. This confirms that rock samples with different extents of damage in laboratory can be made by monotonic

loading. It also can be seen that the number of accumulative micro-cracks at the peak stress point does not change obviously with γ, implying the level of σ_1 at the starting point of unloading phase has little influence on the accumulative rock damage at the peak stress point. Figure 9b presents the sum of micro-cracks and relevant generation rate of micro-crack during the unloading phase. The generation rate u_c of micro-crack is calculated by dividing the sum of micro-cracks by the elapsed time steps during the unloading phase. It can be found that as γ increases, the sum of micro-cracks at the unloading phase roughly shows a downward trend, while the generation rate u_c generally increases with γ, which implies that the total damage in the unloading phase gradually decreases with the increase in level of σ_1 at the initial unloading point, but the corresponding damaging process becomes more violent. Figure 9c presents the ratio between the amounts of tensile micro-cracks and shear micro-cracks versus γ. It can be seen that the ratio is larger than 150 in all cases, indicating that the microscopic failure mechanism of rock sample is mainly tensile cracking. As γ increases, the ratio at the pre-peak or unloading phase gradually decreases and the decreasing rate relevant to $\gamma < 0.8$ is much higher than that in other cases, which implies that under this unloading condition, the grain-scale shear dislocation tends to occur in rock when the level of σ_1 at the initial unloading point is relatively low.

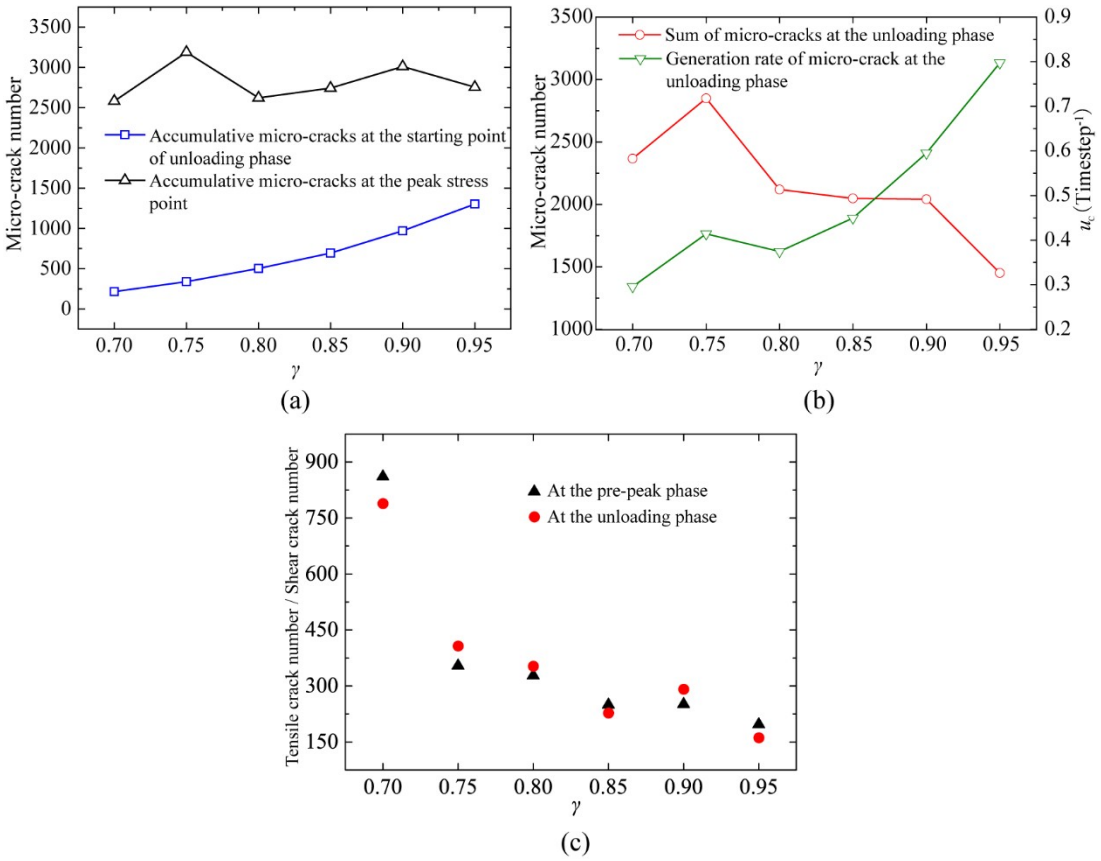

FIGURE 9 Micro-crack characteristics **(a)** sum of micro-cracks at the key stress points **(b)** accumulative micro-cracks and generation of micro-crack during the unloading phase **(c)** ratio between the amount of tensile cracks and shear cracks

4.3 Spatial distribution of particle displacement and micro-cracks

The macro deformation of rock is controlled by the movement of particles that forms the rock, so the mechanism of rock deformation can be further explained by analyzing the movement of particles. In order to better capture the process of particle movement and micro-cracking, four points are identified on the axial stress-strain curves as shown in Figure 8. a and c denote the initial unloading point and peak stress point, respectively. b denotes the midpoint of the unloading phase. d is in the post-peak phase, and the relevant load is 40 percent of the peak strength. Figure 10 presents the spatial distribution of particle displacement and micro-cracks corresponding to these four points. The colored arrows represent particle displacement vectors. It can be seen that the spatial distributions of particle displacement with different γ exhibit

analogous varying trends. Take γ = 0.7 as an example, at point a, the particles at the upper and lower ends of the sample move towards the middle part, making the displacements of particles in middle part lower than those at both ends, and the central section particles that are near both edges tend to be extruded from the sample, which is the mechanism of rock dilatancy under compression. At point b, we can see that the royal blue region in which the displacements of particles are relatively low has been enlarged, and more particles near both edges are nearly extruded. At point c, it should be noted that the royal blue region where the displacements of particles are relatively low has been rotated clockwise by several degrees, with much more particles near both edges being nearly extruded. At point d, it is worth noting that the royal blue region containing particles with lower displacements basically coincides with the macro fracture zone. The directions of particle displacements in the royal blue region or the macro fracture zone are at random, while the displacement vectors of particles on both sides of the macro fracture zone are roughly parallel to the macro fracture, and any two displacement vectors of particles on different sides of the macro fracture zone are opposite in direction. The multi-direction movements of particles belonging to the macro fracture zone contribute to explaining the generation of micro-cracks concentrated in the macro fracture zone. Further analyses show that before point c, the royal blue region containing particles with lower displacements shrinks with the increase in γ, which implies that a higher level of σ_1 at the initial unloading point will make the overall difference in displacements of particles greater. Additionally, it can be seen from Figure 10 that the spatial distribution of micro-cracks is influenced by the parameter γ. At point a, the density of micro-cracks in space is proportionate to the parameter γ. When γ is lower than 0.8, the micro-cracks are fairly scatter. Nevertheless, when γ is higher than 0.85, a preferential cracking region containing the largest gathering of micro-cracks can be observed in the sample. As axial strain increases, more and more micro-cracks arise and form the preferential cracking region or make the preferential cracking region thicker and clearer. At point c, it should be noted that the difference between micro-crack densities in space with various γ is

minimal. Following a rapid growth in micro-cracks at the post-peak stage, the macro fracture bands are eventually formed along the preferential cracking regions.

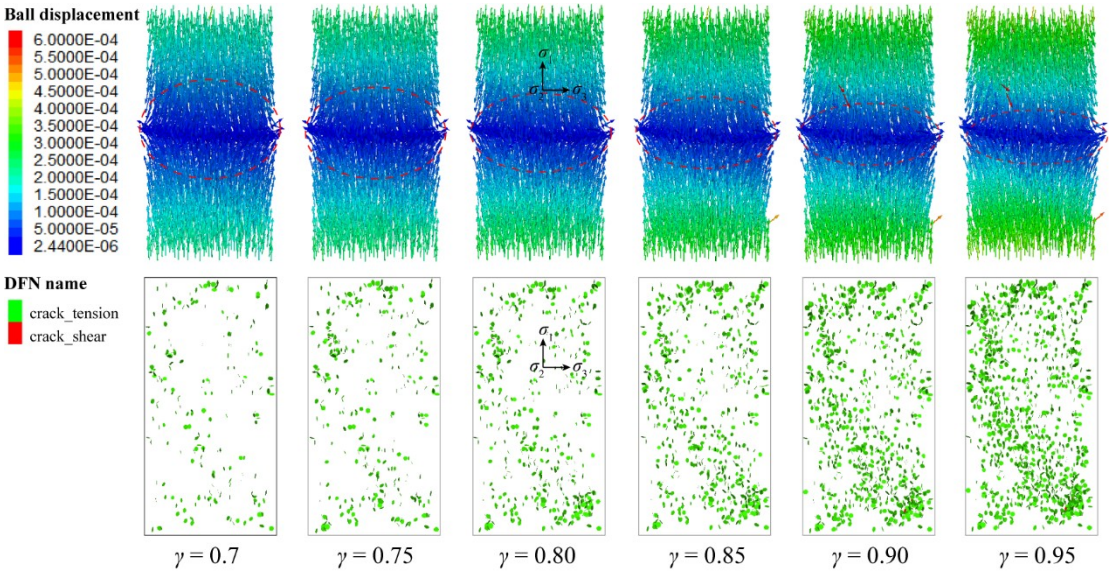

(a)

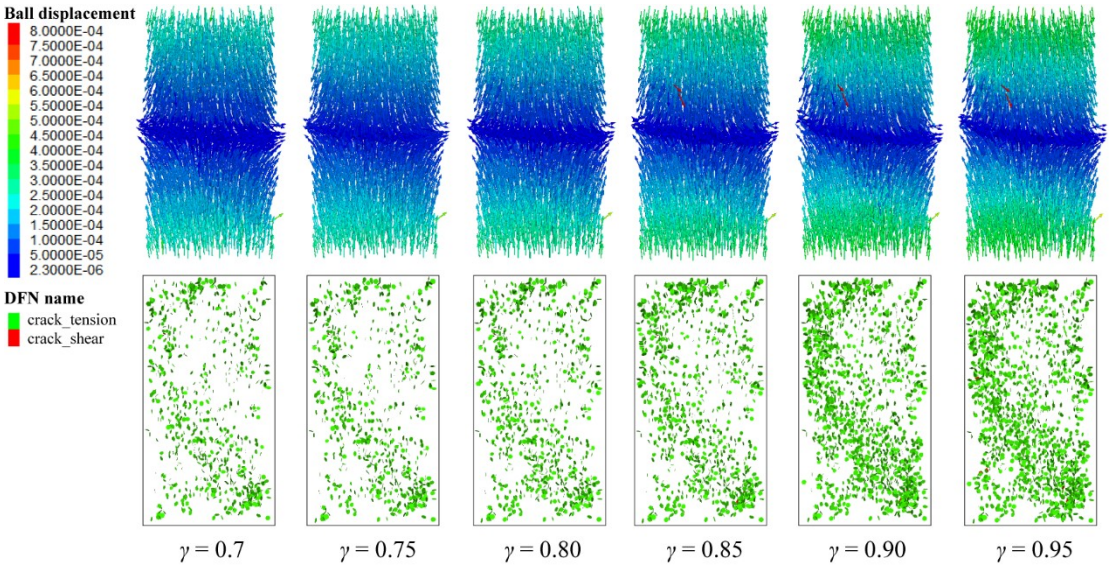

(b)

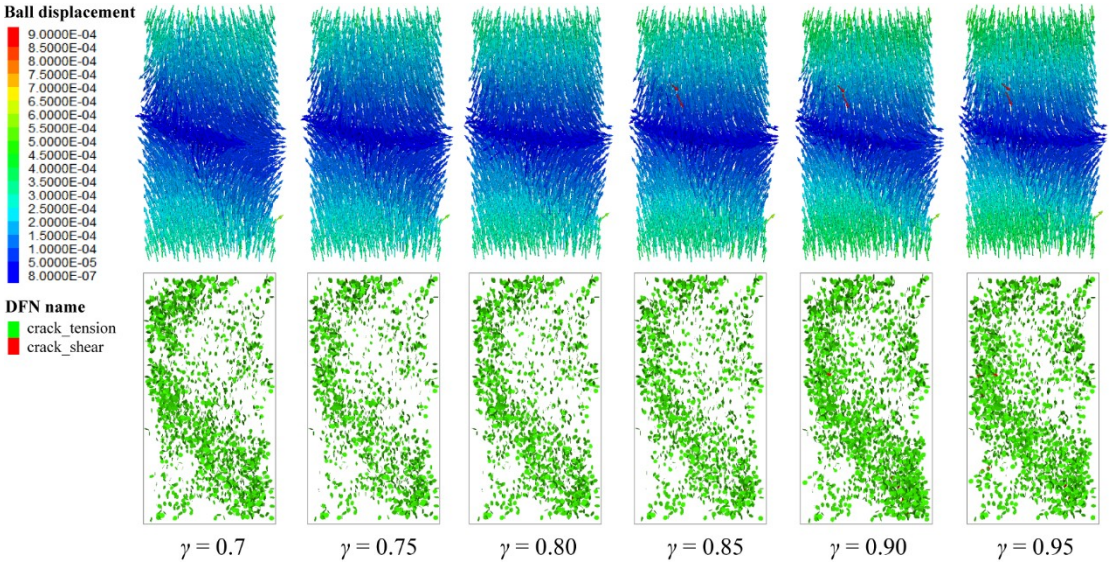

(c)

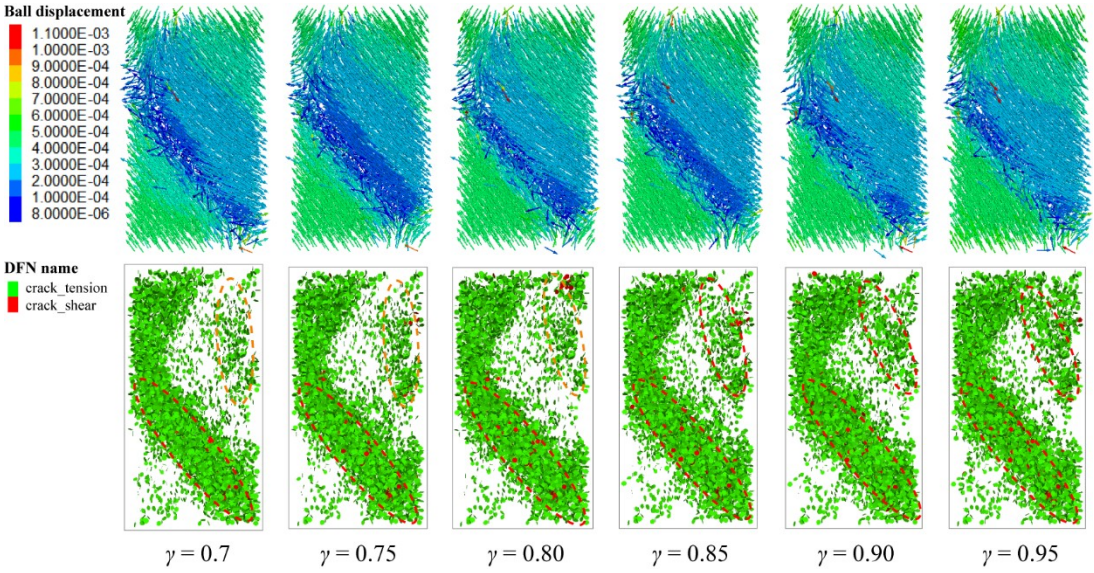

(d)

FIGURE 10 Spatial distribution of particle displacement and micro-cracks

4.4 Microscopic interpretation of the formation of macro fracture

So far the failure mode of brittle rock under various stress conditions has been extensively investigated by researchers.[43-49] Xu et al[19] also pointed out that under true-triaxial unloading conditions, the level of σ_1 at the initial unloading point had an influence on the transition of rock failure mode. However, few studies have been made to yield insights on the mechanism of macro fracture. In view of this, further

statistical analyses of the simulation data are conducted in this section for the microscopic interpretation of the formation of macro fracture.

Figure 11 presents the probability density functions of micro-crack dip for numerical samples corresponding to above-mentioned four loading points. The micro-crack dip refers to the angle (no more than 90°) between the plane where micro-crack is located and the horizontal plane. As seen in Figure 11, there is no obvious difference between the probability density functions of micro-crack dip with different γ. Take γ = 0.7 as an example, at point a, the probability density function is proportionate to the micro-crack dip. The micro-crack dips ranging from 80° to 90° are dominant in probability density function, while the probability density functions of micro-crack dips less than 50° are close to zero. With the increase in axial strain, the percentage of micro-cracks with a dip lower than 50° gradually increases, meanwhile, the accumulative probability of micro-crack dips ranging from 80° to 90° decreases. At point d, it can be seen that the probability density function almost increases linearly with the micro-crack dip, indicating that micro-cracks with various dips have been generated at the post-peak phase. This should be attributed to the multi-direction movements of particles in the macro fracture zone. Figure 12 presents the rose diagrams of micro-crack dip direction for numerical samples corresponding to above-mentioned four loading points. The micro-crack dip direction in present study is measured in a clockwise direction from the positive direction of the y-axis. At point a, it can be observed that the dip directions of micro cracks with different γ are mainly distributed in the interval of 75°~105° or 255°~285°, indicating that the dominant dip direction is 90° or 270°, which is consistent with the direction of σ_3. With the increase in axial strain, the shapes of rose diagrams for micro-crack dip directions change from strip to cobble, and the frequencies of micro-crack dip direction around 90° or 270° decrease gradually. Another feature worth noting is that there are some difference among the rose diagrams for micro-crack dip directions with different γ. With the increase in γ, the frequencies of micro-crack dip direction around 90° or 270° show a decreasing trend. However, as axial strain increases, the

discrepancy among rose diagrams with different γ decreases gradually.

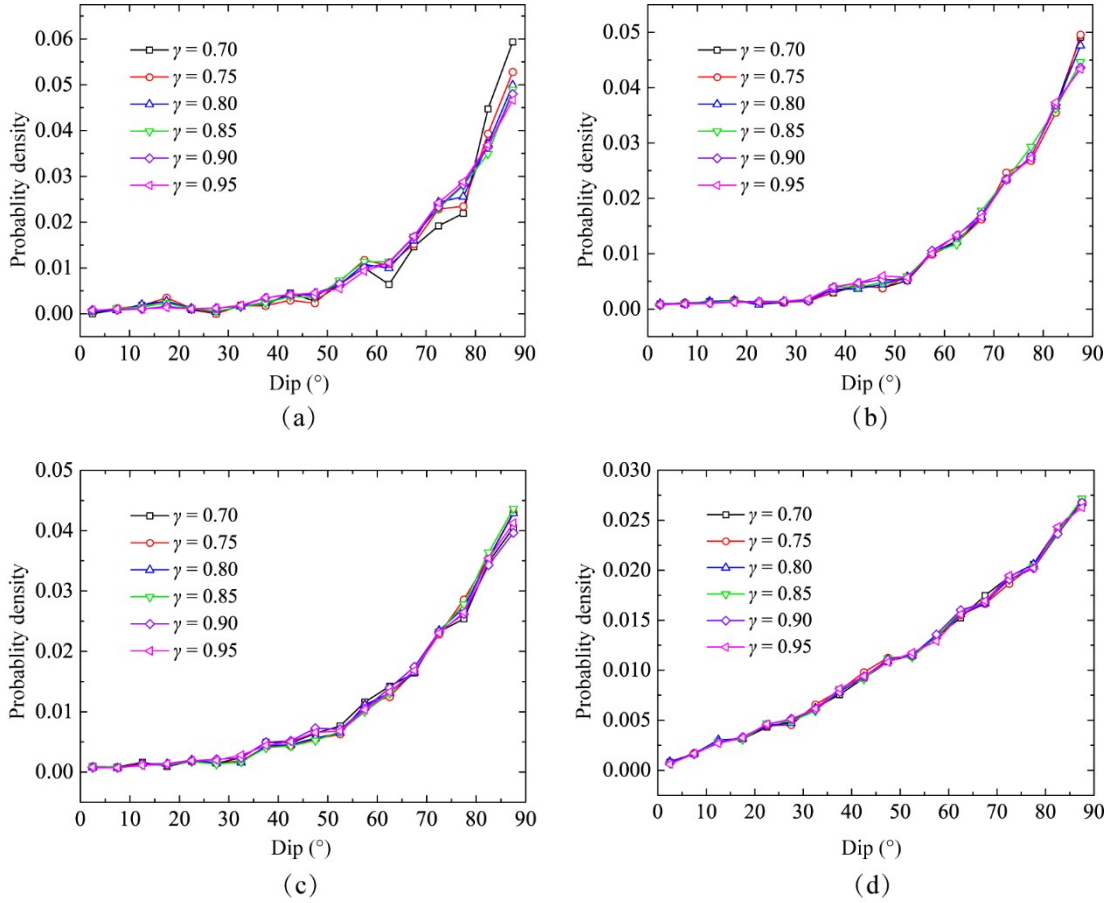

FIGURE 11 Probability density functions of micro-crack dip

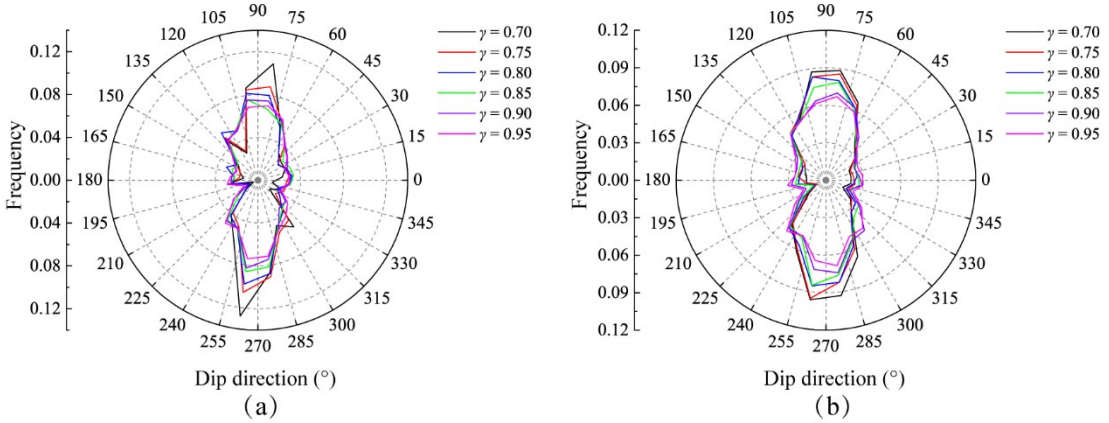

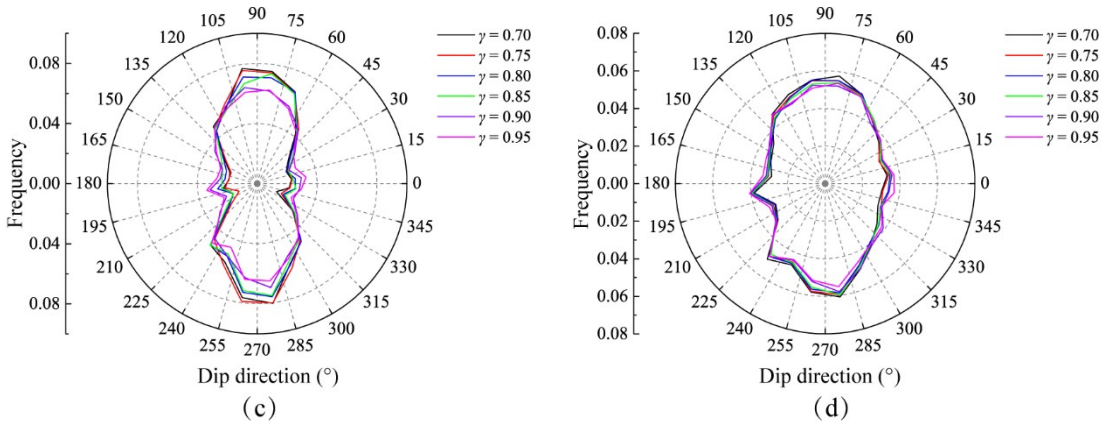

FIGURE 12 Distribution of micro-crack dip direction

According to the spatial distribution of micro-cracks for numerical samples, before the formation of macro fracture band, most of the micro-cracks arise along a nearly vertical or vertical direction and the corresponding dip directions mainly coincide with the direction of σ_3. Moreover, almost all the micro-cracks in the samples are tensile micro-cracks. One can speculate from these findings that at the initial stage of physical experiments, the mineral grains squeeze each other in the direction of σ_1 under true-triaxial compression. Owning to less constraints in the direction of σ_3, neighboring mineral grains on the similar level horizontally are most likely to generate the largest relative displacement in the direction of σ_3, so the cements between these mineral grains break first, inducing the occurrence of primary micro-cracks with steep dip angles, as illustrated in Figure 13. Due to inhomogeneity of sandstone, micro-cracks firstly appear in the relatively weak cements. As a result, the primary micro-cracks distribute randomly at the initial stage of experiments. Once the weaker cements are destroyed, the mineral grains on both sides of these cements move apart in opposite directions, increasing the relative distances between the mineral grains initially affected and other mineral grains around them, which leads to the breakage of cements around the mineral grains involved in the primary micro-cracks. Therefore, clusters of micro-cracks are generated along the primary micro-cracks. With the development of micro-crack clusters and micro-cracks caused by inhomogeneity of rock, a preferential cracking region containing the largest gathering of micro-cracks is gradually formed. The previously generated micro-cracks will cause large deformation or stress concentration in neighboring cements. Therefore,

much more micro-cracks will occur in the preferential cracking region at an alarming rate, resulting in the ultimate macro fracture band with a clear boundary. Compared with the micro-cracks appearing at the initial stage of experiments, the later micro-cracks are more likely to be induced by the disturbance from adjacent micro-cracks, so the orientations of later micro-cracks tend to be more random. It can be used as an explanation for the variations of micro-crack dip and dip direction with the axial strain in Figure 11 and Figure 12.

For sandstone samples with different γ, one of the primary features about failure mode is that when γ is relatively small, both macro shear and tensile fractures can be observed in the samples. As seen from Figure 10, at point a, micro-cracks have been aggregated to form the preferential cracking region in the upper right part of sample if γ is relatively high, subsequent σ_3 reduction can hardly alter the type of ultimate macro fracture whose location is restricted by the preferential cracking region, so only shear macro fracture occurs in the upper right part of sample. However, when γ is relatively small, the upper-right shear macro fracture is replaced by tensile macro fracture. To yield insights on the transition of failure mode with increasing γ, we present the distribution of contacts in tension and corresponding contact force in Figure 14. The contacts are first projected onto the σ_2-σ_3 plane and the contact angle is measured in an anticlockwise direction from the projection line of contact to the contact axis. It can be seen that at pre-peak stage, almost all the angles of contacts in tension are distributed in the interval of 165°~195° or 345°~15°, indicating that the angles of contacts in tension have a preferential horizontal orientation. At point d, the statistical curve for contact angles have rotated clockwise by several degrees. It is worth noting that at point a, the number of contacts in tension with different contact angles and corresponding contact force are basically proportionate to the parameter γ. However, with the increase in axial strain, the increasing rates of contact number and corresponding contact force in tension with a relatively low γ are generally larger than those with higher γ. At point b, the contacts in tension corresponding to $\gamma = 0.7$ are the most, which implies that during the unloading phase, more contacts change from

compressive state into tensile state in the sample with a relatively low γ. Moreover, the corresponding contact fore relevant to $\gamma = 0.7$ is the largest at point c. A superiority in tensile contacts between particles when γ is relatively low makes the particles more likely move toward both sides and causes the difference between the preferential cracking regions with different γ. As a result, the approximately vertical fracture forms in the upper right part of sample when γ is relatively low.

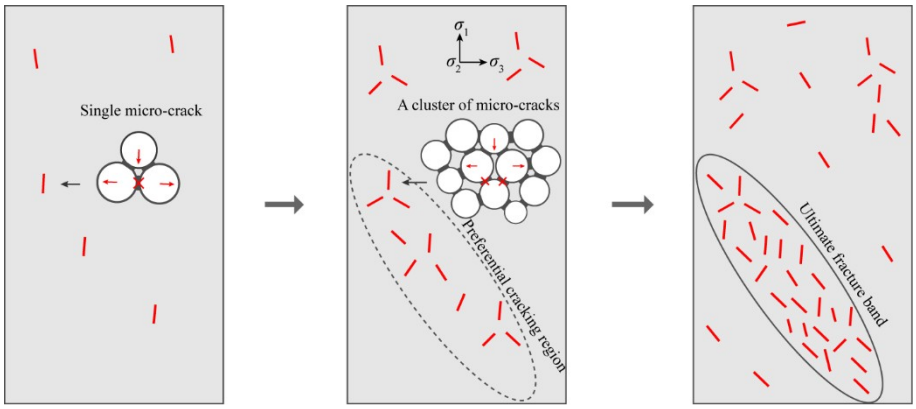

FIGURE 13 Interpretation of macroscopic failure (red line represents micro-crack)

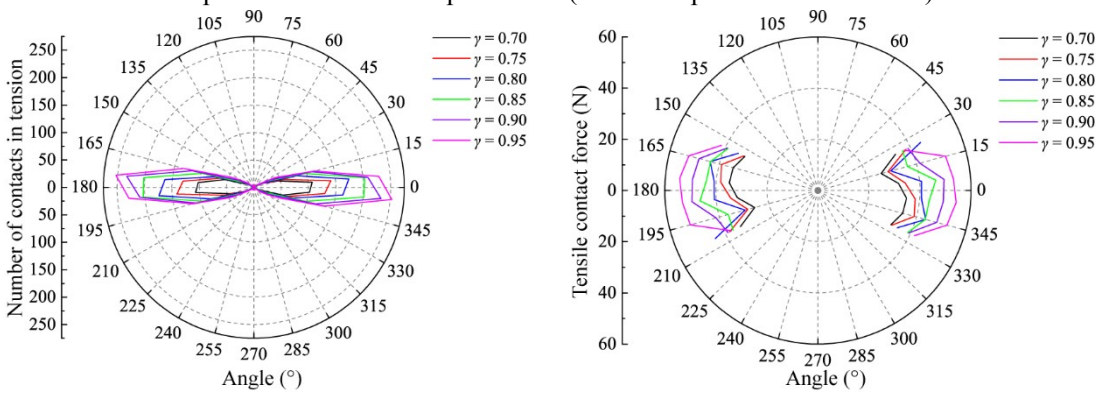

(a)

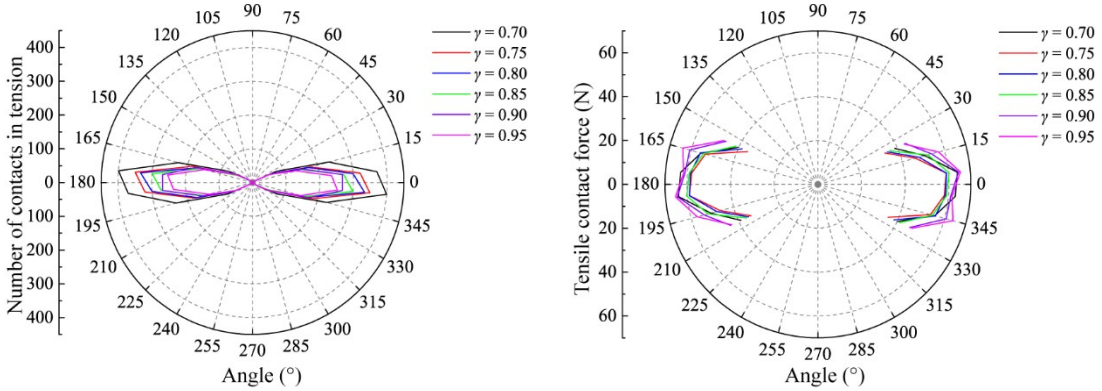

(b)

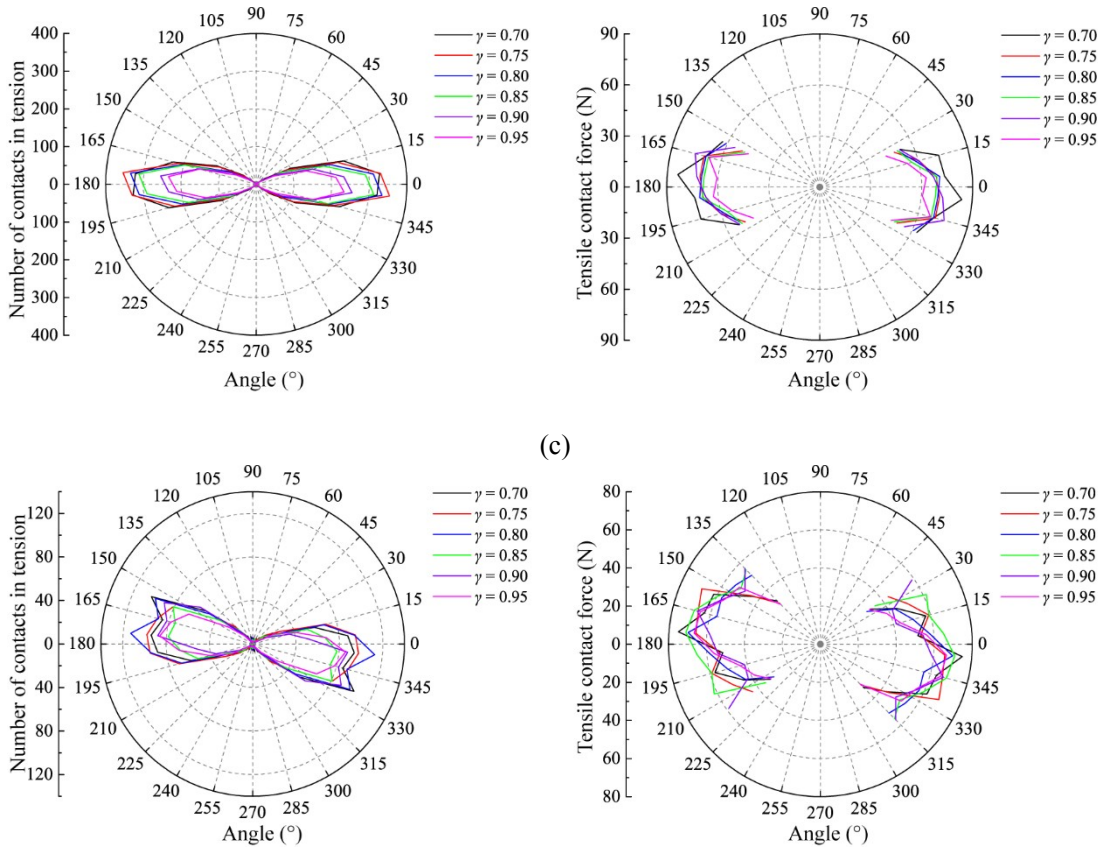

(c)

(d)

FIGURE 14 Distribution of contact in tension and corresponding contact force

5 Conclusions

In this study, the mechanical behaviors and failure characteristics of sandstone samples under true-triaxial unloading conditions with different maximum principal stress levels were comprehensively investigated by laboratory tests and DEM simulations. A comparison was firstly made between the macroscopic mechanical behaviors obtained from the laboratory experiments and numerical simulations. Detailed analyses were then conducted in terms of the micro-cracks characteristics and particle displacement to reveal the microscopic mechanism of rock deformation and failure. The following conclusions can be drawn：

(1) The maximum principal stress level at the initial unloading point has an influence on the true-triaxial unloading behaviors of sandstone samples. As the level of σ_1

at the initial unloading point increases, the ultimate bearing capacity of sandstone sample is increasingly strengthened, while the sample collapses more easily during the unloading process, and the failure mode of sandstone sample changes from mixed tensile-shear failure to shear failure.

(2) Under true-triaxial unloading conditions, the micro-crack count rates of sandstone samples experience a faster growth at the unloading stage compared with those at the former stages and reach a maximum after the peak stress point. As the level of σ_1 increases, the accumulative micro-cracks at the unloading point and micro-crack generation rate during the unloading phase exhibit an increasing trend, while the sum of micro-cracks at the unloading phase and the ratio between the amount of tensile micro-cracks and shear micro-cracks roughly show a downward trend.

(3) At the unloading point, the displacements of particles in middle part of sandstone samples are lower than those at both ends. As the axial strain increases, the region where the displacements of particles are relatively low is gradually rotated and finally coincides with the macro fracture zone in which the directions of particle displacements are at random.

(4) The formation of macro fracture in sandstone sample is closely related to the stress conditions and material inhomogeneity. Due to material inhomogeneity and less constraints in the direction of σ_3, the randomly distributed micro-cracks more likely arise along a nearly vertical or vertical direction at the initial stage of testing and corresponding dip directions basically coincide with the direction of σ_3. As the axial strain increases, previously generated micro-cracks cause large deformation or stress concentration in neighboring cements of rock samples, inducing more micro-cracks nearby, which finally results in the formation of ultimate macro fracture band. The approximately vertical fracture in the upper right part of sample when γ is relatively low should be attributed to the superiority in tensile contacts between particles in terms of contact number and corresponding tensile force.

Authorship contribution statement

Xiao Fan: Conceptualization, Methodology, Investigation, Writing - original draft. Jiang De-Yi: Resources, Software, Methodology, Writing - original draft, Supervision. Wu Fei: Conceptualization, Methodology, Writing - original draft. Chen Jie: Software, Data curation, Formal analysis. Zhang Jian-Zhi: Investigation, Formal analysis, Data curation. Liu Wei: Writing - editing, Validation.

Acknowledgments The work was financially supported by the National Science and Technology Major Project (2016ZX05045001-005), the National Key Research and Development Plan (2017YFC0804202), National Natural Science Foundation of China (No.51704044), General Projects of Basic Science and Frontier Technology Research Projects of Chongqing Science and Technology Planning Project (No. cstc2017jcyjAX0264). The authors would like to acknowledge their financial contribution and convey their appreciation to these organizations for supporting this basic research.

Compliance with ethical standards

Conflicts of interest The authors declare that they have no conflict of interest.

References

1. Su G, Jiang JQ, Zhai SB, Zhang G. Influence of tunnel axis stress on strainburst: An experimental study. *Rock Mech Rock Eng*. 2017;50(6):1551–1567.
2. Cai M. Influence of intermediate principal stress on rock fracturing and strength near excavation boundaries—Insight from numerical modeling. *Int J Rock Mech Min Sci*. 2008;45(5):763–772.
3. Zhang JZ, Zhou XP, Zhou LS, Berto F. Progressive failure of brittle rocks with non-isometric flaws: Insights from acousto-optic-mechanical (AOM) data. *Fatigue Fract Eng Mater Struct*. 2019;42(8):1787–1802.
4. Zhou XP, Niu Y, Zhang JZ, Shen XC, Zheng Y, Berto F. Experimental study on effects of

freeze-thaw fatigue damage on the cracking behaviors of sandstone containing two unparallel fissures. *Fatigue Fract Eng Mater Struct*. 2019;42(6):1322–1340.

5. Chen HD, Cheng YP, Zhou HX, Li W. Damage and permeability development in coal during unloading. *Rock Mech Rock Eng*. 2013;46(6):1377–1390.
6. Xiao F, Jiang DY, Wu F, Zou QL, Chen J, Chen B, Sun ZG. Effects of prior cyclic loading damage on failure characteristics of sandstone under true-triaxial unloading conditions. *Int J Rock Mech Min Sci*. 2020;132:104379.
7. Qiu SL, Feng XT, Xiao JQ, Zhang CQ. An experimental study on the pre-peak unloading damage evolution of marble. *Rock Mech Rock Eng*. 2014,47(2):401–419.
8. Xue Y, Ranjith P G, Gao F, Zhang D, Cheng H, Chong Z, Hou P. Mechanical behaviour and permeability evolution of gas-containing coal from unloading confining pressure tests. *J Nat Gas Sci Eng*. 2017;40:336–346.
9. Ding QL, Ju F, Mao XB, Ma D, Yu BY, Song SB. Experimental investigation of the mechanical behavior in unloading conditions of sandstone after high-temperature treatment. *Rock Mech Rock Eng*. 2016;49(7):2641–2653.
10. Huang RQ, Huang D. Evolution of rock cracks under unloading condition. *Rock Mech Rock Eng*. 2014;47(2):453–466.
11. Zhou KP, Liu TY, Hu ZX. Exploration of damage evolution in marble due to lateral unloading using nuclear magnetic resonance. *Eng Geol*. 2018;244:75–85.
12. Wu W, Zhao Z, Duan K. Unloading-induced instability of a simulated granular fault and implications for excavation-induced seismicity. *Tunn Undergr Sp Tech*. 2017;63:154–161.
13. Feng XT, Zhang X, Kong R, Wang G. A novel mogi type true triaxial testing apparatus and its use to obtain complete stress–strain curves of hard rocks. *Rock Mech Rock Eng*. 2016;49(5):1649–1662.
14. Feng XT, Zhao J, Zhang XW, Kong R. A novel true triaxial apparatus for studying the time-dependent behaviour of hard rocks under high stress. *Rock Mech Rock Eng*. 2018;51(9):2653–2667.
15. Li XB, Du K, Li DY. True triaxial strength and failure modes of cubic rock specimens with unloading the minor principal stress. *Rock Mech Rock Eng*. 2015;48(6):2185–2196.
16. Du K, Tao M, Li XB, Zhou J. Experimental study of slabbing and rockburst induced by true-

triaxial unloading and local dynamic disturbance. *Rock Mech Rock Eng*. 2016;49(9):3437–3453.

17. He MC, Miao JL, Feng JL. Rock burst process of limestone and its acoustic emission characteristics under true-triaxial unloading conditions. *Int J Rock Mech Min Sci*. 2010;47(2):286–298.
18. Zhao XG, Wang J, Cai M, Cheng C, Ma LK, Su R, Zhao F, Li DJ. Influence of unloading rate on the strainburst characteristics of beishan granite under true-triaxial unloading conditions. *Rock Mech Rock Eng*. 2014;47(2):467–483.
19. Xu H, Feng XT, Yang C, Zhang X, Zhou Y, Wang Z. Influence of initial stresses and unloading rates on the deformation and failure mechanism of Jinping marble under true triaxial compression. *Int J Rock Mech Min Sci*. 2019;117:90–104.
20. Zhang JZ, Zhou XP, Yin P. Visco-plastic deformation analysis of rock tunnels based on fractional derivatives. *Tunn Undergr Sp Tech*. 2019;85:209–219.
21. Shen H, Zhang Q, Li Q, Li X, Shi L, Shen N. Experimental and numerical investigations of the dynamic permeability evolution of a fracture in granite during shearing under different normal stress conditions. *Rock Mech Rock Eng*. 2020;53(10):4429–4447.
22. Zhou Y, Sheng Q, Li N, Fu XD. Numerical investigation of the deformation properties of rock materials subjected to cyclic compression by the finite element method. *Soil Dyn Earthq Eng*. 2019;126:105795.
23. Beer G, B.A. Poulsen. Efficient numerical modelling of faulted rock using the boundary element method. *Int J Rock Mech Min Sci & Geomech Abst,* 1994;31(5):485–506.
24. Gong J, Nie Z, Zhu Y, Liang Z, Xiang W. Exploring the effects of particle shape and content of fines on the shear behavior of sand-fines mixtures via the DEM. *Comput Geotech*. 2018;106:161–176.
25. Tang JZ, Yang SQ, Zhao YL, Tian WL. Experimental and numerical modeling of the shear behavior of filled rough joints. *Comput Geotech*. 2020;121:103479.
26. Yang SQ, Tian WL, Huang YH, Ranjith PG, Ju Y. An experimental and numerical study on cracking behavior of brittle sandstone containing two non-coplanar fissures under uniaxial compression. *Rock Mech Rock Eng*. 2016;49(4):1497–1515.
27. Hazzard JF, Young RP. Simulating acoustic emissions in bonded-particle models of rock. *Int*

J Rock Mech Min Sci. 2000;37(5):867–872.

28. Liu G, Cai M, Huang M. Mechanical properties of brittle rock governed by micro-geometric heterogeneity. *Comput Geotech*. 2018;104:358–372.
29. Park B, Min KB. Bonded-particle discrete element modeling of mechanical behavior of transversely isotropic rock. *Int J Rock Mech Min Sci*. 2015;76:243–255.
30. Bahaaddini, M. Effect of boundary condition on the shear behaviour of rock joints in the direct shear test. *Rock Mech Rock Eng*. 2017;50(5):1141–1155.
31. Bahaaddini M, Sharrock G, Hebblewhite BK. Numerical direct shear tests to model the shear behaviour of rock joints. *Comput Geotech*. 2013;51:101–115.
32. Park JW, Song JJ. Numerical simulation of a direct shear test on a rock joint using a bonded-particle model. *Int J Rock Mech Min Sci*. 2009;46(8):1315–1328.
33. Wang P, Cai M, Ren F, Li C, Yang T. A digital image-based discrete fracture network model and its numerical investigation of direct shear tests. *Rock Mech Rock Eng*. 2017;50(7):1801–1816.
34. Duan K, Kwok CY, Ma X. DEM simulations of sandstone under true triaxial compressive tests. *Acta Geotech*. 2017;12(3):495–510.
35. Bai Q, Young RP. Numerical investigation of the mechanical and damage behaviors of veined gneiss during true-triaxial stress path loading by simulation of in situ conditions. *Rock Mech Rock Eng*. 2019;53(1):133–151.
36. Bieniawski ZT, Bernede MJ. Suggested methods for determining the uniaxial compressive strength and deformability of rock materials. *Int J Rock Mech Min Sci & Geomech Abst.* 1979;16(2):138–140.
37. ITASCA. Particle flow code, version 5.0Z. Minneapolis, MN, USA: Itasca: 2015.
38. Zhang S, Wu S, Duan K. Study on the deformation and strength characteristics of hard rock under true triaxial stress state using bonded-particle model. *Comput Geotech*. 2019;112:1–16.
39. De Simone M, Souza L M S, Roehl D. Estimating DEM microparameters for uniaxial compression simulation with genetic programming. *Int J Rock Mech Min Sci*. 2019;118:33–41.
40. Cheng H, Shuku T, Thoeni K, Yamamoto H. Probabilistic calibration of discrete element simulations using the sequential quasi-monte carlo filter. *Granul Matter*. 2018;20(1):11.

41. Yoon J. Application of experimental design and optimization to PFC model calibration in uniaxial compression simulation. *Int J Rock Mech Min Sci*. 2007;44(6):871–889.
42. Zhou XP, Zhang JZ, Qian QH, Niu Y. Experimental investigation of progressive cracking processes in granite under uniaxial loading using digital imaging and AE techniques. *J Struct Geol*. 2019;126:129–145.
43. Kong B, Wang E, Li Z, Wang X, Liu J, Li N. Fracture mechanical behavior of sandstone subjected to high-temperature treatment and its acoustic emission characteristics under uniaxial compression conditions. *Rock Mech Rock Eng*. 2016;49(12):1–8.
44. Duan K, Ji Y, Wu W, Kwok CY. Unloading-induced failure of brittle rock and implications for excavation-induced strain burst. *Tunn Undergr Sp Tech*. 2019;84:495–506.
45. Feng XT, Kong R, Zhang XW, Yang C. Experimental study of failure differences in hard rock under true triaxial compression. *Rock Mech Rock Eng*. 2019;52:2109–2122.
46. Wu F, Chen J, Zou QL. A nonlinear creep damage model for salt rock. *Int J Damage Mech*, 2018;28(5):758–771.
47. Wu F, Gao RB, Zou QL, Chen J, Liu W, Peng K. Long-term strength determination and nonlinear creep damage constitutive model of salt rock based on multi-stage creep test: Implications for underground natural gas storage in salt cavern. *Energy Sci Eng*. 2020;00:1–12.
48. Zhang JZ, Zhou XP. AE event rate characteristics of flawed granite: From damage stress to ultimate failure. *Geophys J Int.* 2020;222(2):795–814.
49. Zhang JZ, Zhou XP. Forecasting catastrophic rupture in brittle rocks using precursory AE time series. J Geophys Res: Sol Ea, 2020;125(8):e2019JB019276. https://doi.org/10.1029/2019JB019276.